A VLT/FORS2 NARROWBAND IMAGING SEARCH FOR MG II EMISSION AROUND $z \sim 0.7$ GALAXIES

Ryan Rickards Vaught,[1,2] Kate H. R. Rubin,[1] Fabrizio Arrigoni Battaia,[3] J. Xavier Prochaska,[4] and Joseph Hennawi[5]

[1] Department of Astronomy, San Diego State University, San Diego, CA 92182

[2] Center for Astrophysics and Space Sciences, Department of Physics, University of California, San Diego, CA

[3] Max-Planck-Institut fur Astronomie, Konigstuhl 17, D- 69117 Heidelberg, Germany

[4] Astronomy & Astrophysics, UC Santa Cruz, 1156 High St., Santa Cruz, CA 95064 USA

[5] Department of Physics, Broida Hall, University of California, Santa Barbara, CA 93106-9530

ABSTRACT

The mass and energy of galactic winds remain poorly constrained via traditional absorption line studies. One way to better constrain these parameters is to measure the spatial extent of the outflow in emission. We perform a VLT/FORS2 narrowband imaging of 5 star-forming galaxies at redshift $z = 0.67 - 0.69$ in the GOODS-S field as part of an effort to spatially resolve and constrain the radial extent of large-scale outflows traced by Mg II emission. These observations probe extended Mg II emission down to unmatched surface brightness limits of 5.74×10^{-19} ergs sec $^{-1}$ cm^{-2} arcsec^2 (5σ). We do not detect any extended Mg II emission in any of our galaxies, thus placing strong upper limits on the strength of Mg II emission in the sample galaxies. Our observations allow us to create the first ever spatially-resolved map of Mg II absorption, revealing approximately constant absorption strengths across the galaxy disks. Our detection limits in concert with a previous studies Keck/LRIS spectra allow us to model Mg II emission for isotropic and anisotropic dust-free winds. We find that anisotropic winds reduce the strength of estimated missing Mg II emission below our 5σ limit.

Keywords: galaxies: evolution, Galactic Winds

1. INTRODUCTION

Galactic winds play a critical role in regulating the star formation rates and stellar masses of galaxies (Werk et al. 2014); however, the physical mechanism that powers these galactic winds remains uncertain. Some possible mechanics have been proposed by theoretical studies that include thermal pressure from core collapse supernova, radiation pressure from starbursts and finally cosmic ray pressure (Larson 1974; Chevalier & Clegg 1985; Springel & Hernquist 2003; Sugahara et al. 2017). Additionally, the impact galactic winds have on their host galaxies (i.e, their mass and energy content) has remained difficult to constrain with observations.

An accurate picture of what types of galaxies host outflows comes from numerous absorption line studies of galaxies (Veilleux et al. 2005; Weiner et al. 2009; Martin

Corresponding author: Ryan Rickards Vaught
rjrickar@ucsd.edu

et al. 2012; Rubin et al. 2014). Outflows are detected by measuring the blueshift (outflow) or redshift (inflow) of absorption transitions with respect to the host galaxy systematic velocity. Spectroscopy of galaxies from low to high redshifts probing cold gas ($T \lesssim 10^4$ K) which absorbs in Na I and cool gas ($T \sim 10^4$ K) in Mg II has revealed outflows in most galaxies that host active star-formation (e.g. Chen et al. 2010; Martin et al. 2012; Rubin et al. 2014). Even though these probes can constrain: the radial velocity, column density and covering fraction of the flow, this method is weak in constraining the overall radial extent and provides no information on the morphology of the outflow.

One way of developing these constraints is to trace the extent of winds in emission. This has been demonstrated using rest-frame optical transitions (i.e Hα, [O III], etc) as tracers for winds around nearby starbursts (Matsubayashi et al. 2009; Veilleux et al. 2009; Tripp et al. 2011) as these transitions can trace the warm shock heated phase of the gas. A novel, alternative transition poten-

tially useful for tracing winds in emission is the Mg II $\lambda\lambda 2976, 2803$ doublet in the rest-frame ultraviolet (UV) (Weiner et al. 2009; Kornei et al. 2013). While most studies of winds using Mg II have focused on its absorption kinematics, Rubin et al. (2011) recently observed strong Mg II emission with a P-Cygni line profile in the spectrum of a strongly star-forming galaxy at redshift $z = 0.694$. This emission was the first detection of an outflow beyond the spatial extent of the galaxy continuum in the distant universe, with a minimum spatial extent > 7 kpc.

One proposed production mechanism for the galaxy's observed Mg II line profile is photon scattering. In this mechanism, Mg II ions in the region of the wind closest to the observer will absorb continuum photons in the resonant transitions, λ_{2796} and λ_{2803}. Once these transitions are excited, they may only decay back to the ground state and if the optical depth of the gas is high, then the gas will resonantly trap the absorbed photons. Because the photons are absorbed in the rest frame of the gas, the absorption will be blueshifted relative to the galaxy's systematic velocity. The Mg II ions in the section of the wind farthest from the observer will absorb and scatter photons that are redshifted relative to the front portion of the wind. Because the photons are redshifted, the photons will be able to travel freely towards the observer through the wind to produce emission at and redward of the systematic velocity of the galaxy (Rubin et al. 2011, Prochaska et al. 2011). Since the first detection of Mg II emission by (Rubin et al. 2011), a further detection of extended Mg II emission is found in Martin et al. (2013), where they observe Mg II emission that extends $12 - 18$ kpc for the galaxy 32016857 at $z = 0.9392$. Additionally, Mg II is found in 1D and IFU spectra (Erb et al. 2012 and Feltre et. al (2018)). In these surveys of galaxies between with redshift $0.70 < z < 2.30$, Mg II is detected in pure emission, pure absorption and with P-Cygni profiles. Detections of Mg II in emission was found to be associated with galaxies of lower stellar mass and bluer spectral slopes.

Various models of galactic winds are explored in Prochaska et al. 2011. This analysis involved generating spectra for the Mg II and Fe II* transitions, using a set of radiative transfer algorithms, for an isotropic and anisotropic set of dust and dust-free winds. The authors demonstrated that isotropic dust-free winds will conserve photon flux, thus predicting that blueshifted absorption lines should be accompanied by emission profiles of winds with similar equivalent widths (EW). Anisotropic winds however were demonstrated to significantly weaken emission at strengths proportional to the angular extent of the wind. The scattered emission

was additionally weakened by the inclusion of dust and the affect of a strong interstellar medium (ISM).

In this paper, we present the first narrowband imaging of Mg II line emission around 5 star-forming galaxies located in the deep Great Observatories Origins Deep Survey south (GOODS-S) field at redshift $z \sim 0.7$. The value in using narrowband imaging is the ability to spatially resolve any absorption and emission from a galaxy. We use two filters: a line filter and a continuum filter. The line filter covers the Mg II doublet, while the continuum filter is off-set from line filter. The continuum filter will allow us to observe the continuum level of the galaxy near the Mg II doublet. With the resulting images taken using the two filters, we can subtract the continuum image from the Mg II image, effectively creating an image that contains only photons from Mg II. Contrary to 1D spectra, the narrowband imaging has the ability to measure the surface brightness, optical depth and radial extent of a wind. This narrowband imaging will allow us to create the first ever spatially resolved map of Mg II emission.

In Section 2 we describe our sample of GOOD-S galaxies, Keck/LRIS spectra as well as our VLT/FORS2 observations, imaging, and absolute flux calibration. We go into detail in our method of image subtraction in Section 3. The analysis of these data are included in Section 4, in detail we discuss the production surface bright profiles and limits for each galaxy, as well as the production of narrowband measured equivalent widths. Section 5 contains the results from our narrowband imaging analysis. We compare our SB detections limits to previous detections of extended Mg II emission, additionally we compare our observations to predictions made by radiative transfer models in Section 6. We conclude this paper in Section 7. We adopt a ΛCDM cosmology with $h_{70} = H_0/(70 \text{ km s}^{-1} \text{ Mpc}^{-1})$, $\Omega_{\rm M} = 0.3$, and $\Omega_\Lambda = 0.7$.

2. OBSERVATIONS AND DATA REDUCTION

2.1. *Sample Selection*

Our target galaxies were selected from a Keck/LRIS survey of UV absorption lines in ≈ 100 objects having redshifts $0.3 < z < 1.4$ and $B_{AB} < 23$ in fields with deep HST/ACS imaging (Rubin et al. 2014). In particular, this parent survey targeted galaxies in a total of nine Keck/LRIS pointings located in both of the GOODS fields (Giavalisco et al. 2004) and the AEGIS survey field (the Extended Groth Strip; Davis et al. 2007). In inspecting the redshift distribution of the portion of this sample observable from the Southern Hemisphere, we uncovered a narrow peak of nine galaxies in the interval $0.66 < z < 0.68$. This peak is in fact the global maximum of the distribution, as all other bins

of width $\Delta z = 0.02$ have at most four galaxies. Moreover, there are two narrow interference filters available on VLT/FORS2 centered at $\lambda \sim 468.4$ and 472.6 nm which cover the Mg II $\lambda\lambda2796, 2803$ transition in precisely this redshift interval. We selected our final sample of five of these galaxies at $0.66 < z < 0.68$ to be close on the sky such that they could be imaged in a single $7' \times 7'$ FORS2 pointing.

The absorption line modeling presented in (Rubin et al. 2014) indicates that these five galaxies are driving strong outflows traced by Mg II with velocities $\sim 150 - 420$ km s^{-1} and equivalent widths (EW) $\sim 2 - 3$ Å. Modeling of the galaxy broad-band spectral energy distributions obtained from multi-wavelength ancillary imaging data yields star formation rates (SFR) ranging from ~ 4 to 40 $M_\odot$ yr^{-1} and stellar masses in the range $\log M_*/M_\odot \sim 9.9 - 11.0$. The properties of the sample, as well as precise target coordinates taken from Rubin et al. (2014), are listed in Table 2.

2.2. VLT/FORS2 Observations

Our barrow-band imaging data were taken in service-mode using the FORS2 instrument on the VLT 8.2m telescope Antu between October 2012 and February 2013. We used two narrowband filters, HeII+47 and HeII/3000+48, that have peak transmission at wavelengths that correspond to the Mg II doublet lines at our sample redshift of $z \sim 0.7$ (see Table 1). The filter transmission curves are plotted along with each galaxy's spectrum in Figure 2.

FORS2 has a pixel scale of $0.25''$ pixel^{-1} and a field of view of $7' \times 7'$ with 2×2 binning. Our observations were carried out under photometric and thin cloud conditions (program ID: 090.A-0427A). The seeing (see Figure 3) ranged from 0.5 arcsec to 2.5 arcsec. The data were taken with three pointings offset by 0.25' East/West with exposure times of ≈ 1000 s. A total of 38 exposures were taken in each filter. Summing the individual exposure times for each filter results in a combined exposure time of 10.0 hours each for the HeII+47 and HeII/3000+48 filters.

2.3. Supplemental Keck/LRIS spectra

In addition to VLT imaging, in the present analysis we utilize galaxy spectra taken from the Rubin et al. (2014) Keck I Low Resolution Imaging Spectrometer (LRIS) program. A $0.9''$ slit width was used for all slitmasks and the median FWHM resolution for the spectra is 274 km s^{-1} at $\lambda_{\mathrm{rest}} \approx 2800$ Å and 286 km s^{-1} at $\lambda_{\mathrm{rest}} \approx 2600$ Å (see Figure 2).

2.4. Image Reduction

The data were reduced using custom routines written in **Python**. The images were first corrected by subtracting and removing the overscan region of the CCD. Then the images were bias-subtracted and flat-fielded using twilight flats. To improve the flat-fielding essential for detecting faint extended emission across the fields, we further correct for the illumination patterns using night-sky flats. The night-sky flats were produced by combining the unregistered science frames with an average sigma-clipping algorithm after masking out all the objects, and any bad pixels. Each individual image was cleaned of cosmic rays and bad pixels by utilizing the *L.A. Cosmic* algorithm (van Dokkum 2001). The astrometry solutions were calculated via Astrometry.net (Lang et al. 2010), yield a standard deviation in the galaxy coordinates of $\sigma \approx 0.10''$. Before image stacking, we ran each frame through *SExtractor* (Bertin et al. 1996) in order to create a root mean square (RMS) map of each science image.

The final stacked image for each filter is obtained using *SWarp* (Bertin et al. 1996). Each individual frame is first sky-subtracted using a background mesh size of 256 pixels which is approximately $64''$. We chose the mesh size to be large enough such that the extended emission is not mistakenly subtracted (Arrigoni Battaia et al. 2015) . The frames, after background-subtraction, are resampled onto a common astrometric solution using a *Lancosz3* interpolation kernel. The images are average-combined and weighted by the night-flat image in order to increase the signal-to-noise of any Mg II emission. Additionally, *SWarp* generates a final set of RMS image from the night flats and the combination of RMS images for individual science frames. Our final stacked images in each filter are shown in Figure 4 with the target galaxies indicated.

Table 1. Filter properties and exposure times of the VLT/FORS2 observations. The width of the transmission curves ($\Delta\lambda$) are calculated by convolving the transmission curve with the total wavelength range of the filter. These values differ slightly from those reported by the European Space Observatory.

Filter	λ_{eff}(Å)[a]	$\Delta\lambda$(Å)	N[b]	$T(s)$[c]	S[d]
HeII+47	4675.21	50.11	38	35,959	2.45
HeII/3000+48	4722.46	44.82	38	36,937	2.40

[a] λ_{eff} is the effective wavelength of the filter transmission curve.
[b] Total number of images
[c] Total exposure time
[d] S, the sensitivity of the filter, is in units of 10^{-17} ergs counts^{-1} cm^{-2}
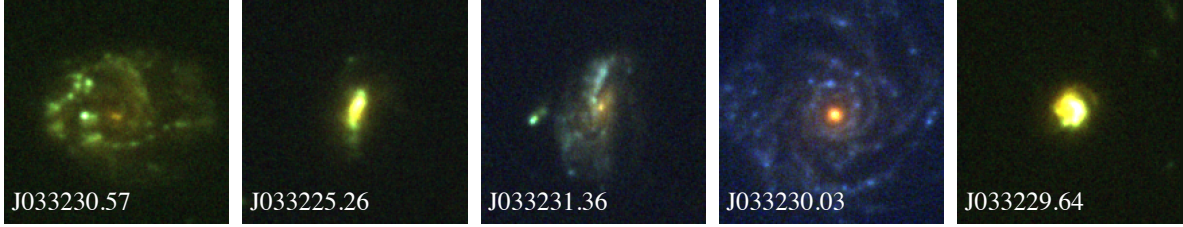
Figure 1. Color imaging of our sample galaxies in the *HST*/ACS F435W, F606W, and F775W filters obtained as part of the GOODS survey (Giavalisco et al. 2004). Each image is 5" × 5".

Table 2. Properties of the 5 galaxies in our sample as estimated in Rubin et al. (2014). The EW (in the observed frame) include both components of the Mg II doublet and were calculated with Eq. 6 and the supplemental Keck/LRIS spectra.

Object	R.A.	Dec	z	SFR($M_\odot$ yr^{-1})	$\log M_*/M_\odot$	EW$_{\rm obs}$(Å)
J033225.26-274524.0	03:32:25.26	-27:45:23.9	0.6660	$9.1^{+1.3}_{-3.7}$	$9.86^{+0.05}_{-0.04}$	7.539 ± 0.354
J033231.36-274725.0	03:32:31.35	-27:47:24.9	0.6669	$10.5^{+1.7}_{-1.6}$	$10.02^{+0.03}_{-0.03}$	5.835 ± 0.493
J033230.03-274347.3	03:32:30.03	-27:43:47.2	0.6679	3.8^{+0}_{-0}	$10.98^{+0.01}_{-0.0}$	12.794 ± 1.710
J033229.64-274242.6	03:32:29.64	-27:42:42.5	0.6671	$40.5^{+8.2}_{-12.1}$	$10.30^{+0.07}_{-0.03}$	13.239 ± 0.263
J033230.57-274518.2	03:32:30.56	-27:45:18.2	0.6807	$12.6^{+1.7}_{-2.1}$	$10.48^{+0.03}_{-0.07}$	6.106 ± 0.370

2.5. *Absolute Flux Calibration*

We acquired observations of the standard star GD50 from archival ESO calibration imaging at 4 independent epochs. Performing aperture photometry at each epoch and airmass, we calculated the atmospheric extinction coefficients (k) to be 0.181 magnitudes for the HeII/3000+48 filter and 0.190 magnitudes for the HeII+47 filter. We perform absolute flux calibration using the methods of Jacoby et al. (1990). We first convolve the spectral energy distribution of the standard star, $F(\lambda)$ in ergs sec^{-1} Å^{-1} cm^{-2}, with that of the known transmission curve of the filter, $T_i(\lambda)$. This yields F_i, the total observable flux in each bandpass filter i with units of ergs sec^{-1} cm^{-2}:

$$F_i = \int F(\lambda)T_i(\lambda)d\lambda.$$

It is not uncommon to assume that $F(\lambda)$ is constant over the small width of the filter. However, our filter transmission curves are sampled at 5 Å intervals which is the same sampling as the spectral energy distribution of the standard star obtained from the ESO archives (WILL CHECK CALSPEC). Therefore we calculate the integral numerically. The system sensitivity, including the defects of the telescope optics and detector response is then given by

$$S_i = \frac{F_i}{C10^{k_i A}},$$

where k_i is the extinction in magnitudes per airmass, A is the airmass for each individual exposure, C is the measured count rate of the standard star and S_i is in units of ergs counts^{-1} cm^{-2}. Before image co-addition, each science image is corrected for atmospheric extinction by multiplying each frame by $10^{k_i A}$. Next, the image is divided by the exposure time, effectively putting the image in units of counts per sec. After co-addition, the images are then multiplied by the appropriate sensitivity factor S_i. This puts the final images in the appropriate flux units, ergs sec $^{-1}$ cm^{-2}.

3. IMAGE SUBTRACTION

3.1. *Spectral Correction*

In preparation for continuum subtraction, we first consider whether the continuum level of each galaxy spectrum changes significantly over the passbands of our two filters. We use the supplementary spectra from (Rubin et al. 2014), to fit the continuum and determine the
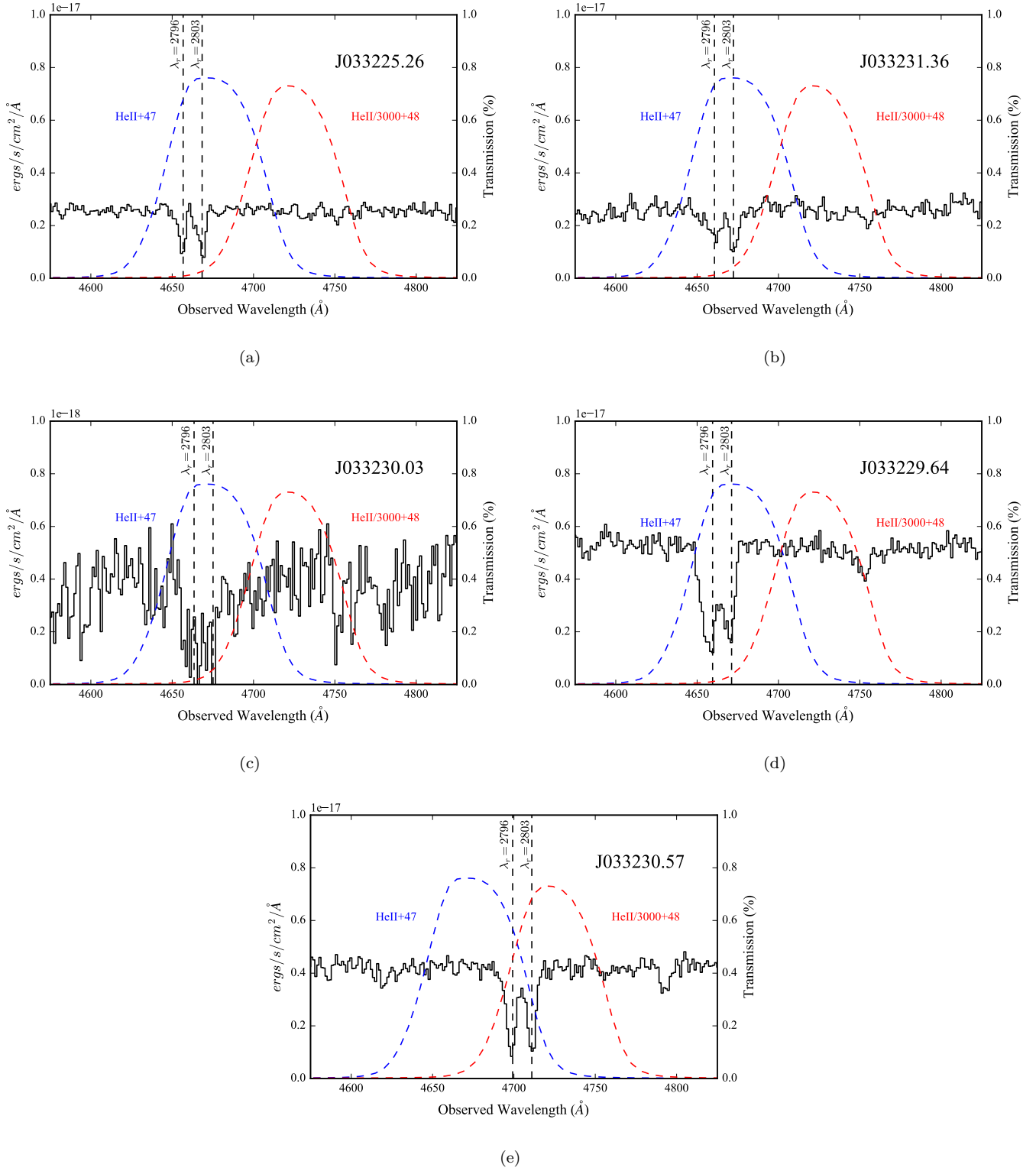
Figure 2. Keck/LRIS spectra of the sample galaxies and the transmission curves of the filters HeII+47 (blue dashed line) and HeII/3000+48 (red dashed line) . The left-hand axis is in units of flux density and the right-hand axis is the percentage of light transmitted the filter at each wavelength. Vertical dashed lines indicate the wavelength of the redshifted Mg II doublet. The Mg II doublet falls fortuitously at the central wavelength of the HEII+47 filter.
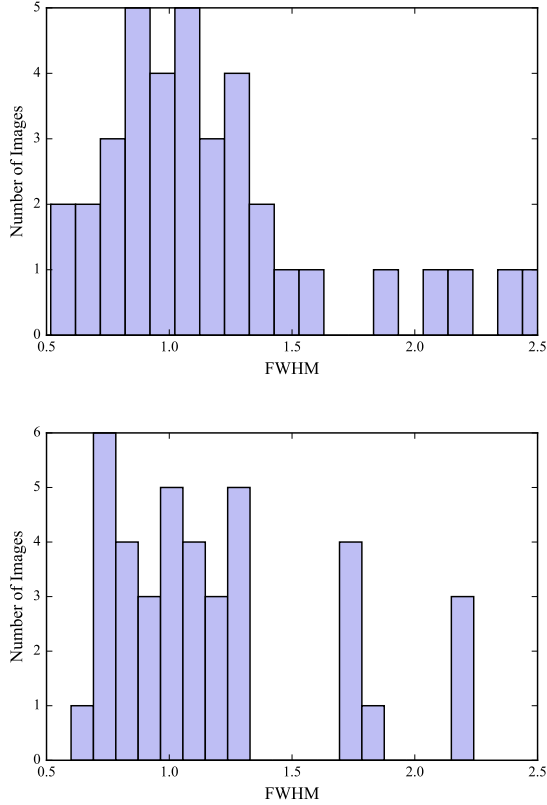
Figure 3. Distribution of seeing conditions for individual exposures comprising our dataset. **Top**: Seeing distribution for the 38 HeII+47 images. The median seeing in this filter is $1.03''$. **Bottom**: Same distribution for the 38 HeII/3000+48 images. The median seeing is $1.08''$. The seeing conditions were calculated by ESO and were provided in the header of each science image.

spectral slope of each galaxy. We use the interactive fitting routine *lt_continuumfit* from the *linetools* package (Prochaska et al. 2016)[1] to fit the continuum. We then find the total continuum flux in each filter by convolving the fitted continuum with each filter's transmission curve. Next, we take the ratio of both integrated totals, as the ratio will indicate the scaling factor needed to correct our flux measurements prior to continuum subtraction. Comparing these ratios between each galaxy, we find that they are effectively the same, within 0.1%, with a value of 1.118. This value is equal to the ratio between the FWHM of the filter transmission curves, allowing us to conclude that the slope of the spectrum of each galaxy is flat, and hence that the continuum level measured in the off-line filter provides an accurate mea-

[1] https://github.com/linetools/linetools

sure of the continuum contribution to the on-line filter flux.

3.2. *Continuum Subtraction*

To properly continuum-subtract the image taken with the on-line filter in excess of the continuum, we follow a prescription given by Arrigoni Battaia et al. (2015). We first determine the continuum flux density from the off-Mg II filter,

$$f_{\rm cont} = \frac{F_{\rm cont}}{\Delta\lambda_{\rm cont}}, \tag{1}$$

where $F_{\rm cont}$ and $\Delta\lambda_{\rm cont}$ are the observed flux per pixel of the continuum image and the transmission FWHM of the continuum filter, respectively. With f_{cont} it is then possible to calculate the flux of any excess emission, $F_{\rm line}$:

$$F_{\rm line} = F_{\rm MgII} - f_{\rm cont}\Delta\lambda_{\rm MgII} \tag{2}$$

where $F_{\rm MgII}$ and $\Delta\lambda_{MgII}$ are the observed flux per pixel in the Mg II filter and the transmission FWHM of the Mg II filter. The continuum subtracted images of each galaxy are shown in Fig. 5. The continuum subtracted image has uniform background and no obvious signatures of emission.

4. ANALYSIS

We have two goals for our study: (1) assess the surface brightness of line emission in the Mg II transition in and around each target galaxy; and (2) spatially resolve the morphology of the strong Mg II absorption observed against the galaxy continua. To reach the both of these goals, we must perform accurate subtraction of the continuum flux of each object from the filter covering the targeted line emission. For four of the five objects in our sample, the HeII+47 image includes both line and continuum emission, and the HeII3000+48 image provides a high S/N measurement of the continuum only ≈ 30 Å redward of the line emission in the rest-frame. We detail below the resulting surface brightness profiles (Section 4.1) and detection limits (Section 4.2) as well at the $\rm EW_{MgII}$ generated from these data (Section 4.3).

4.1. *Surface Brightness Profiles and Limits*

In order to test for the presence of Mg II emission, we perform aperture photometry on the continuum subtracted images using the python library *Photutils*. We choose annuli with a radial thickness of 1 pixel or $0.25''$, such that, $r_{inner} = r_{outer} - 1$ (in pixels). Each annulus is centered on the flux-weighted centroid of the galaxy. By dividing the summed flux in each annulus by the area in arcseconds we produce surface brightness (SB) profiles for each galaxy. These profiles are shown in Figure 6.
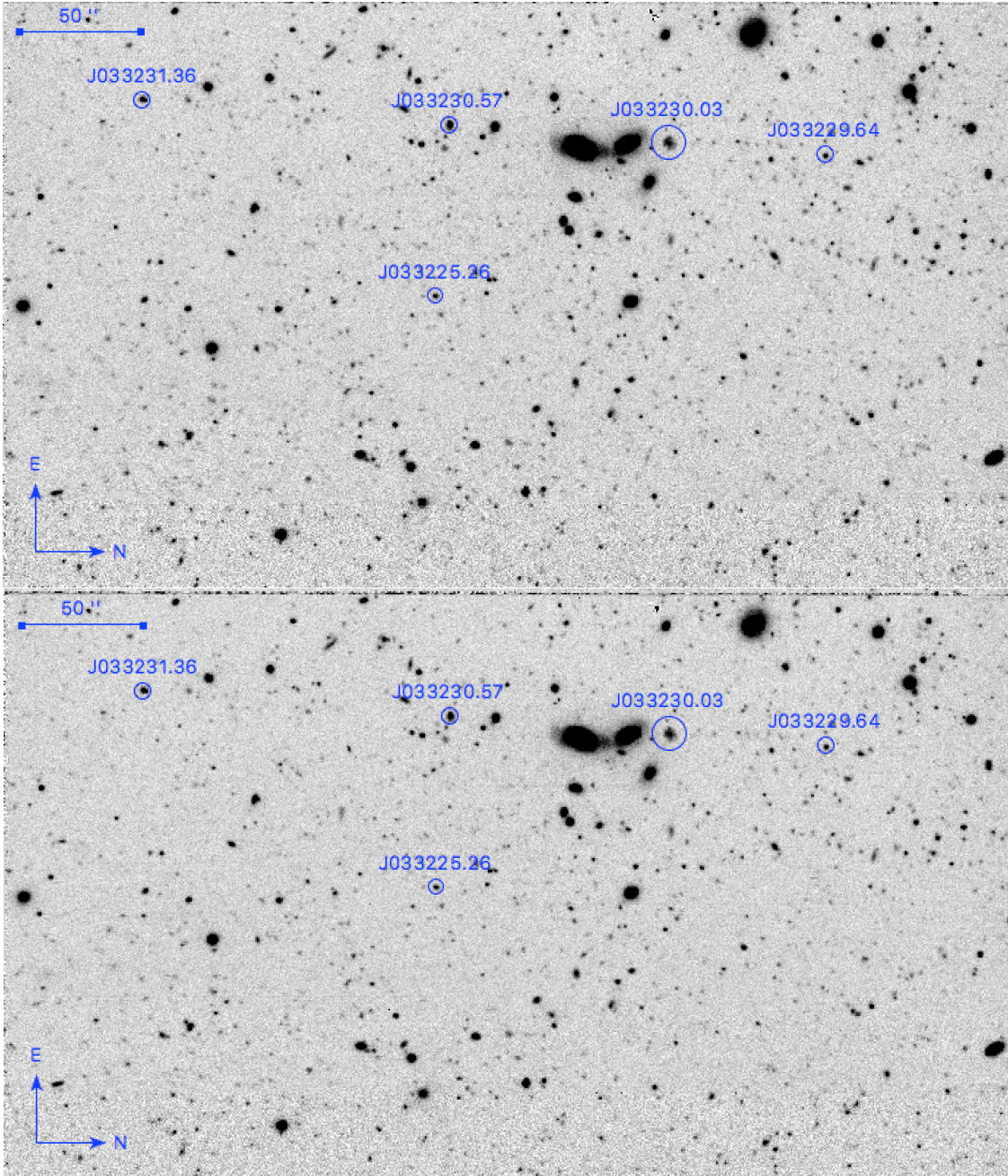
Figure 4. Top: Stacked HeII+47 image of the galaxy sample. Bottom: Stacked HeII3000+48 image of the same pointing. The exposure time of each image is ≈ 10 hours. Each image has a FOV of $7' \times 7'$ which fortuitously contains the full sample of galaxies (indicated by the blue circles). East is up and North is right.

The error in the SB is determined from the stacked RMS images of each object **SWarp**. We place annuli that are identical to the annuli used to find the SB profiles for each galaxy. To calculate the variance inside each annulus, we sum the RMS pixel values in quadrature, then divide by the area of each annulus.

To calculate the 1σ SB limit we follow the procedure of Arrigoni Battaia et al. (2015). We first mask out all the sources, their associated extended halos, and edge noise

in both the HeII+47 and HeII/3000+48 images. We then calculate the RMS of the background in randomly-placed 1" apertures. We convert these RMS values to SB limits *per* 1 sq.arcsec aperture. We find that the 1σ detection limits per 1 arcsec^2 aperture (SB$_1$) are 6.332×10^{-19} ergs sec^{-1} cm^{-2} arcsec^2 and 5.808×10^{-19} ergs sec^{-1} cm^{-2} arcsec^2 in the HeII/3000+48 and HeII+47 filters, respectively. With the 1σ detection limit, SB$_1$, determined for the continuum+Mg II (HeII) image, we
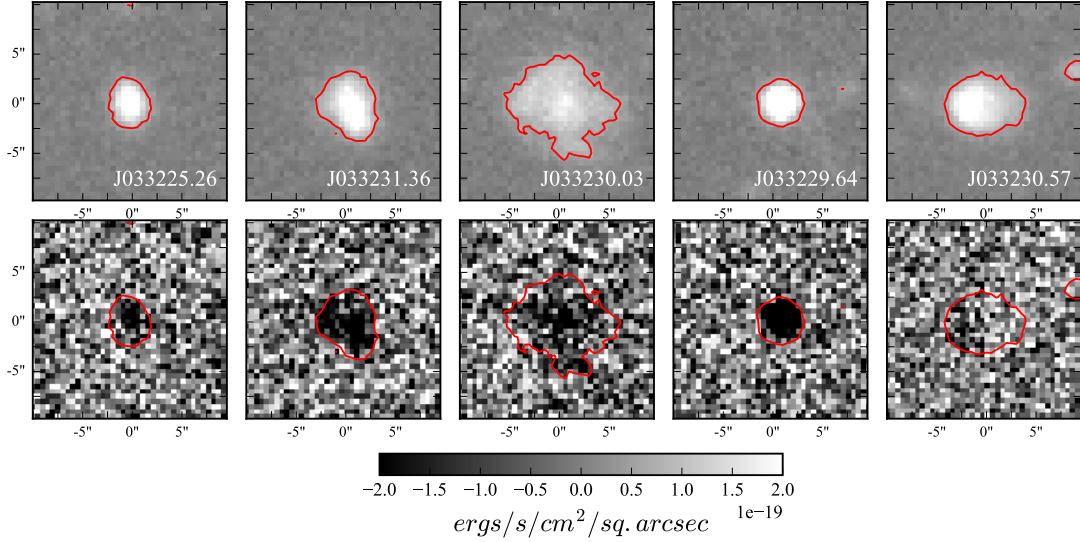
Figure 5. $10'' \times 10''$ images of each galaxy in our sample. Top row: Continuum surface brightness in ergs/s/cm^2/sq.arcsec. Bottom row: Continuum subtracted Mg II surface brightness. Absorption can be seen in 4 of 5 galaxies. The red contours represent the outline of the 1σ surface brightness limit in the HeII/3000+38 image, defined in Sec. 4.1. The colorbar shows the scaling used for the Mg II images.

define a thicker (or "extended") annulus to be used to search for any extended Mg II emission. This extended annulus has an inner radius approximately the size of the SB$_1$ isophotal contour for each galaxy. The outer radius is chosen to be the inner radius plus 5 pixels.

The sensitivity required to detect an extended source depends on its size, as one can reach lower SB levels by spatially averaging over large apertures. In the ideal case of perfect sky subtraction and continuum subtraction, the 1σ SB limit for an extended source is $SB_1/\sqrt{A_{\rm src}}$, where $A_{\rm src}$ is the area in arcsec^2 and SB_1 is the surface brightness limit per 1 arcsec^2 aperture. In practice, the actual detection limits are affected by systematics from imperfect subtraction. Therefore, we empirically determine the limits as follows. We mask all the artifacts and sources in the continuum-subtracted images. Next, we generate randomly sized apertures, place them at random, and extract the fluxes, $F_{\rm src}$, within these apertures. In the ideal case that the sky and continuum are perfectly subtracted, the fluxes, $F_{\rm src}$, from many random apertures should follow a Gaussian distribution with a width of $\sigma_{\rm src} \equiv SB_1\sqrt{A_{\rm src}}$. The distribution of $F_{\rm src}$ for these apertures are shown in Figure 7. We calculate the variance and mean of the distribution and find that Gaussian width, $\sigma'_{\rm src} = 1.1$, of the distribution is broader than $\sigma_{\rm src}$. We adopt $F_{\rm limit} \equiv \sigma'_{\rm src}$ as the 1σ upper limit on the total line flux of extended Mg II emission. The SB$_{\rm limit}$ is just $F_{\rm limit}/A_{\rm src}$. The values of $F_{\rm src}$ and the 5SB$_{\rm limit}$ for each galaxy are listed in Table 3.

Table 3. Significance of extracted flux and detection limits

Object	$F_{\rm src}$(Mg II)[a]	5SB$_{\rm limit}$[b]	Area[c]
J033225.26-274524.0	2.44(0.92)	6.51	21
J033232.36-274725.0	-1.40(-0.53)	6.51	21
J033230.03-274347.3	-5.23(-1.75)	5.74	27
J033229.64-274242.5	1.23 (0.44)	6.22	26
J033230.57-274518.2	-2.53 (-1.00)	6.81	18

[a]Mg II flux is in 10^{-18} ergs sec^{-1} cm^{-2}. The value in the parenthesis is the statistical significance with respect to $\sigma_{\rm src}$
[b]Limits are in 10^{-19} ergs sec^{-1} cm^{-2} arcsec^2
[c]Area of the extended annulus in sq.arcsec

4.2. Test of Surface Brightness Limits

In order to show that our detection limits are reasonable, we simulate emission with varying intensities. The results of this exercise are shown in Figure 8. For each galaxy, we assign our simulated emission a constant surface brightness corresponding to 0, 1, 3, 5, 10 and 20 times the 1σ SB$_{\rm limit}$ inside the largest annulus used (i.e., the extended annulus). Additionally, we assume Gaussian noise with 1σ equal to 1SB$_{\rm limit}$. After placing the simulated emission around the galaxy, we subtract the continuum in the same manner as explained in Section 3.

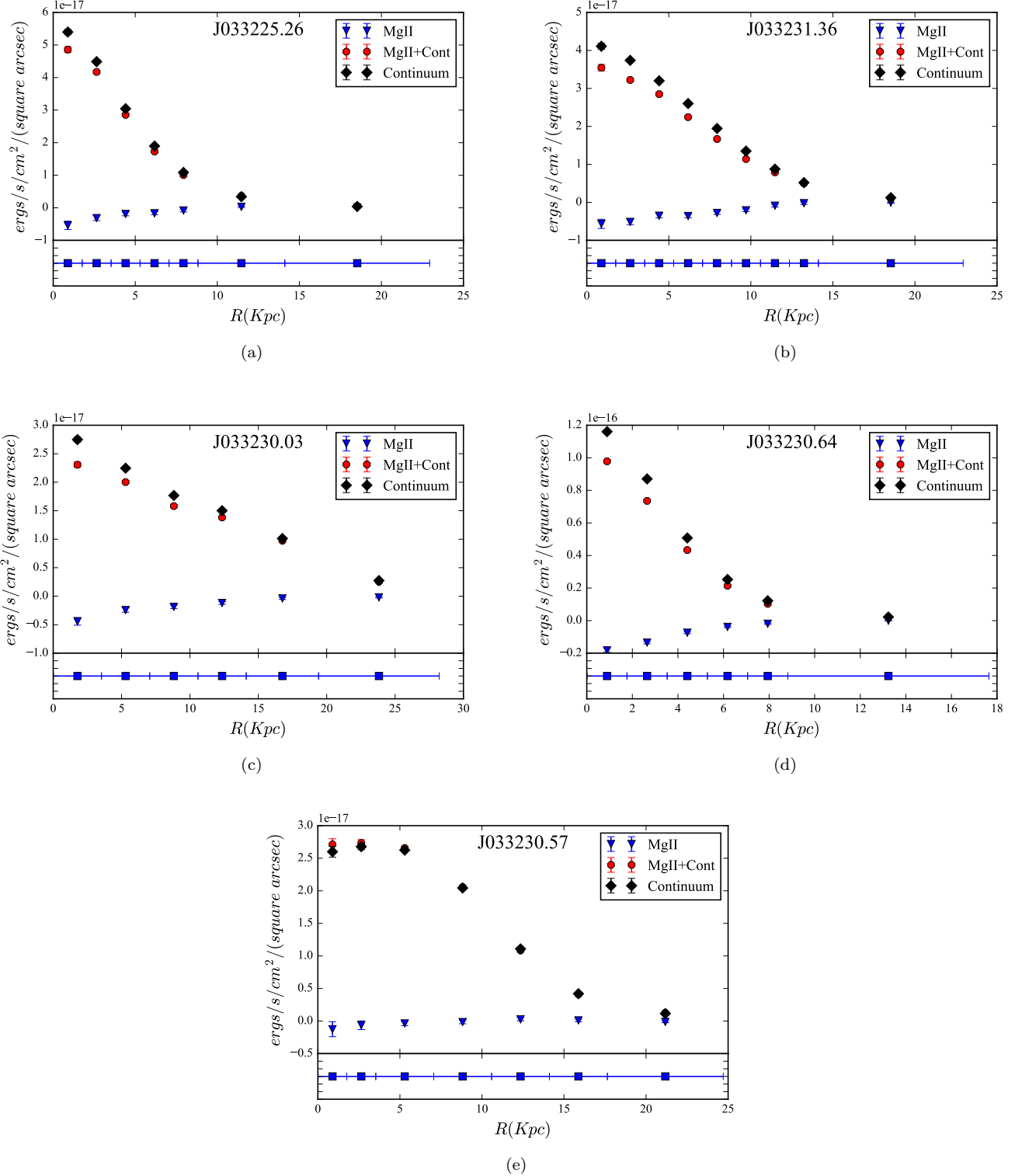We then construct a smoothed χ image following the techniques in Hennawi & Prochaska (2013) and Arrigoni

Figure 6. SB profiles for our sample galaxies. (Top panel) Continuum SB (black) measured for each galaxy. The green points show the Mg II + continuum SB measured for the galaxy in the pre-continuum subtracted image. The blue points show the Mg II line SB measured for the galaxy in the continuum subtracted line emission image.The profile exhibits SB decrements from Mg II absorption. Photometry was performed in circular annuli. (Bottom panel) The vertical hashes in the bottom show the inner and outer radius of each annulus in kpc. Distance from the center of the galaxy (x-axis) is computed using the average value of the inner and outer radii of each annulus.
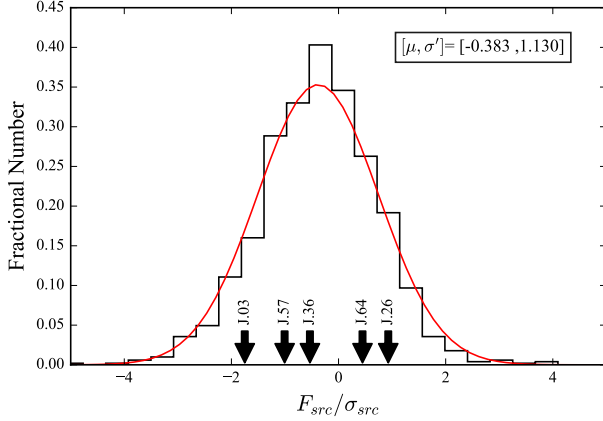
Figure 7. Normalized distribution of F_{src}/σ_{src} values for random circular annuli placed on the continuum-subtracted line image. F_{src} is the total flux within an aperture and σ_{src} is the expected 1σ flux limit in the ideal case of perfect sky and continuum subtraction, i.e $SB_1\sqrt{A_{src}}$. The black arrows point to the statistical significance of the flux inside the "extended annulus" of each galaxy.

Battaia et al. (2015). First, we smooth the continuum-subtracted image:

$$I_{smth} = CONVOLVE[NB\text{-}CONTINUUM], \quad (3)$$

where the CONVOLVE operation indicates convolution of the images with a Gaussian kernel with FWHM=1.5 pixels. Next, we computed the sigma image (σ_{smth}) for the smoothed image (I_{smth}) by propagating the noise image of the unsmoothed data:

$$\sigma_{smth} = \sqrt{CONVOLVE^2[\sigma_{unsmth}^2]}, \quad (4)$$

where the CONVOLVE^2 operation indicates the convolution of the noise image with the square of the Gaussian kernel. The smoothed χ image is defined by

$$\chi_{smth} = \frac{I_{smth}}{\sigma_{smth}}. \quad (5)$$

This χ_{smth} image aids in recognizing the presence of extended Mg II emission.

Figure 8 shows the χ_{smth} images for the 5 levels of simulated Mg II emission. We also include the χ_{smth} image of each galaxy without any simulated emission (in the left most column). Galaxies are outlined by a black isophotal contour corresponding to $1SB_1$ and the simulated emission is contained inside an annulus surrounding each contour. The χ_{smth} images confirm that we should be able to detect extended Mg II emission down to a conservative level of $5SB_{limit}$. Note again that the SB_{limit} does indeed take into account the systematics from imperfect continuum subtraction.

4.3. Equivalent Widths

Here we derive an expression to calculate the equivalent width (EW_{MgII}) of any absorption or emission features observed in our narrow-band imaging. Starting from the expression for EW used in the context of spectroscopy,

$$EW_\lambda = \int (1 - \frac{f_\lambda}{f_{cont}})d\lambda \quad (6)$$

we begin by dividing Eq 2 by the flux density of the continuum and the FWHM of the on-line filter,

$$\frac{F_\lambda}{f_{cont}\Delta\lambda_{MgII}} = \frac{F_{MgII}}{f_{cont}\Delta\lambda_{MgII}} - 1. \quad (7)$$

Next, we rearrange the above expression such that we produce the argument of the integrand in Eq. 6 on the right hand side,

$$-\frac{F_\lambda}{f_{cont}\Delta\lambda_{MgII}} = 1 - \frac{f_{MgII}}{f_{cont}}. \quad (8)$$

We then approximate the integration in Eq. 6 by multiplying the integrand above by the FWHM of the on-line filter $d\lambda = \Delta\lambda_{MgII}$,

$$-\frac{F_\lambda}{f_{cont}} = (1 - \frac{f_{MgII}}{f_{cont}})\Delta\lambda_{MgII}; \quad (9)$$

such that

$$EW_{MgII} = -\frac{F_{MgII}}{f_{cont}}. \quad (10)$$

Using the above equation along with the continuum and continuum-subtracted images, we produce images of the observed-frame EW_{MgII}'s. The observed-frame EW_{MgII} images are displayed in Figures 10, 11, 12, 13, 14, [**WILL CONSOLIDATE THESE FIGURES**] and show only the EWs within the 1σ SB_1 contours of the corresponding Mg II images (prior to continuum subtraction).

To compare our map of EW_{MgII}'s to the values measured from the Keck/LRIS spectra, we place 0.9 arcsec wide apertures on top of each galaxy. The width and angle of the apertures replicate the orientation of the slits used to obtain the spectra. Next, we determine which pixels lie outside the 1σ SB_1 contours and set their values to zero. Outside this contour, the EW_{MgII}'s become poorly constrained due to the lack of S/N in the continuum. We then apply a S/N = 1.5 cut to the continuum image and create a histogram to show the distribution of EW_{MgII}'s inside the contour. The histograms are shown in Figures 10 through 14. Having removed EW_{MgII}'s with low-S/N continuum values from our images, we compute the mean equivalent width inside the Keck/LRIS apertures. These values are summarized in Table 4.
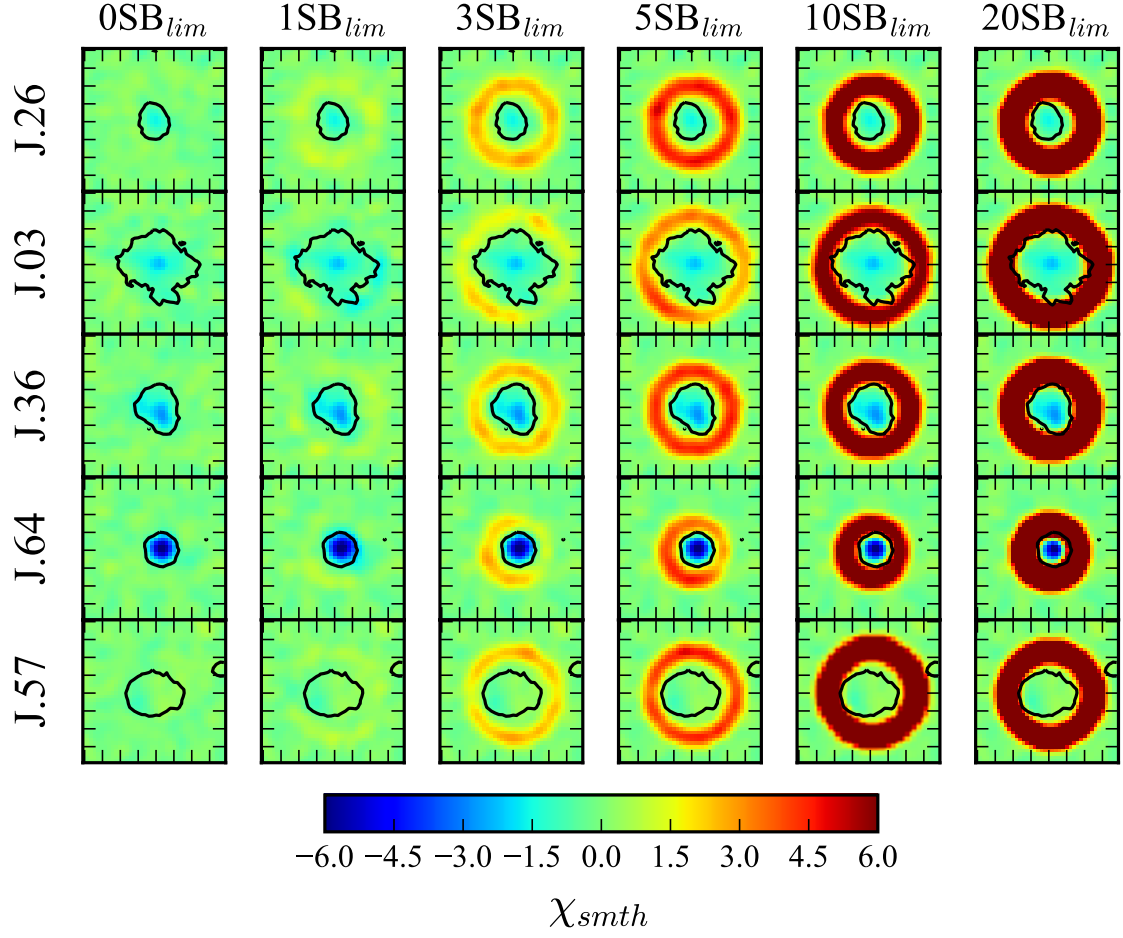
Figure 8. Postage stamp χ_{smth} images of the 5 galaxies in our sample. Every galaxy is placed in the same row in each column. The columns show simulated emission, with levels of 0, 1, 3, 5, 10, and 20 times SB_{lim}. Each postage stamp has a size of $5'' \times 5''$ (corresponding to 35 kpc $\times$ 35 kpc at $z \sim 0.70$). Each stamp shows the galaxy along with the same isophotal contour used in previous figures.

To assess the morphology of the Mg II absorption, we determine the distance of each pixel from the center of each galaxy in kiloparsecs. We plot the EW_{MgII}'s over this projected distance for each galaxy in Figures 10 through 14. Although some of the plots suggest a slight upward trend in the values of the EW_{MgII} with increasing radii, we cannot be confident in this trend because of the large scatter. To better visualize the data and test the significance of the trend, we bin the data radially in 3-5 kpc bins. For example, in Figure 13, the EW_{MgII} from absorption of J033230.03 extends out to $\sim$ 25 kpc. The EW_{MgII}'s are binned in 5 kpc increments. We calculate the mean and scatter of the EW_{MgII}'s in each bin and show these values in Figure 15.

5. RESULTS

5.1. *Spatially Resolved Maps of Mg II Absorption*

In this section we discuss the details of the absorption detected in our SB profiles as well as compare our EW_{MgII} measurements to those measured in the supplemental Keck/LRIS spectra.

5.1.1. *Mg II absorption in surface brightness profiles*

Although we do not detect any extended Mg II emission, we do observe a decrement of flux in the SB profiles of 4 out of 5 galaxies in our sample. Figure 6 shows the SB profiles for the 5 galaxies in our sample. Absorption from Mg II ions is prevalent in the profiles between 10 - 25 kpc, decreasing radially outward from the maximum absorption at the center of the galaxies. In Table 4 we report for the galaxies: J033225.26, J033231.36 and J033230.03 a maximum decrement in the SB profile due to absorption $\sim$ -5.00×10^{-18} erg s^{-1} cm^{-2} per sq.arcsec. Additionally, we report for galaxy J033229.64 a decrement one order of magnitude greater then the previous galaxies with a value of -18.2 ± 0.127 ×10^{-18} erg s^{-1} cm^{-2} per sq.arcsec. Finally, for galaxy J033230.57 the absorption decrement is strongest at the center of the galaxy with a SB value of -1.25 ± 1.15 10^{-18} erg s^{-1} cm^{-2} per sq.arcsec. However, the measured SB of this decrement including error is consistent with measuring zero absorption. The measurement of zero absorption for J033230.57 was expected. Figure 2 shows the KECK/LRIS spectrum of J033230.57 and the transmission curves of the filters HeII+47 and HeII/3000+48. The Mg II transitions of the galaxy are equally sampled by both of our filters. When we subtract the continuum image from the Mg II image we are effectively subtracting the Mg II as well. This measurement suggests that the quality of our subtraction is satisfactory. Because of the lack of absorption we exclude this galaxy from our discussion.

The surface brightness profiles presented in Figures 6 do not exhibit any signs of extended Mg II emission.

5.1.2. *Morphology of MgII Absorption*

Figures 10 through 14 show the images, distributions and radial projections of Mg II EWs. We have zeroed out any values that lie outside the SB_1 contours for each galaxy. We also impose a signal-to-noise cut, only including EWs where the continuum S/N is greater than 1.5. The mean EW is computed for all pixels inside each Keck/LRIS aperture, defined in Sec. 4.3, and the resulting values are summarized in Table 4. Comparing our narrowband EWs with those measured from the spectra, we find good agreement to within a few σ for galaxies J033225.26 and J033232.36, and statistically significant differences for galaxies J033230.03, J033229.64 and J033230.57. We discuss possible causes for these differences below.

Figure 2(c) shows the Keck/LRIS spectrum of galaxy J033230.03. The continuum observed near the Mg II transition is noisy, compared to the spectra of the rest of the sample. Since the value of the EW is dependent on the level of the continuum present near the Mg II transition, it may well be that our choice of continuum level in calculting the EW from the spectrum might be over-estimating the EW of the doublet.

Figure 2(d) shows the Keck/LRIS spectrum of galaxy J033229.64. This galaxy is the brightest galaxy in the sample, suggestive of a bright ISM, which causes the redder transition to almost leak out of the HeII+47 transmission curve. This suggests that it our Mg II images are not measuring the most redward absorption feature, thus underestimating the value of the EW.

In the case of J033230.57 we can easily understand why the EW measured is not in agreement with the spectral EW. Figure 6 shows the SB profile coverage of J033230.57. In this galaxy's profile we do not detect any significant SB decrements, due to absorption, as the two filters cover the Mg II as discussed above. Any signal of absorption in the EW images arises from noise. Figure 5.1.2 shows that the radial projection of the EWs measured for this galaxy that are centered around zero.

To get a better sense of how the EW of Mg II absorption changes with radius as well as account for the effects of seeing, $FWHM \sim 7kpc$, we bin the EWs in radial bins with 5, 4 or 3 kpc widths as shown in Figures through . A majority of the galaxies exhibit large scatter in the binned EWs out to larger radii. To better understand the significance of these trends, we construct a plot that compiles the mean EWs for all the galaxies, shown in Figure 15. To take into account the varying

size of the galaxies, we normalize the distances by the approximate radius of the SB_1 contour for each galaxy.

Upon inspection of Figure 15, we see that all the galaxies exhibit a constant mean EW inside our $1SB_1$ isophotal radius, and suggestive that the covering fraction is also constant across the surface.

5.2. *Limits on MgII Emission*

We do not detect any significant amount of Mg II emission in any of our target galaxies. The χ_{smth} images shown in Figure 8 confirm this. A comparison of the simulated emission with the χ_{smth} image of the original continuum-subtracted image, shown in the first column, similarly suggests that we do not detect any extended Mg II emission. We thus place 5σ upper limits on Mg II emission for each galaxy in the sample, summarized in Table 3. The most sensitive detection limit using the largest area is SB(Mg II) = 5.74×10^{-19} ergs sec $^{-1}$ cm^{-2} arcsec^2, computed for the galaxy J033230.03. Our least sensitive detection limit is SB(Mg II) = 6.81×10^{-19} ergs sec $^{-1}$ cm^{-2} arcsec^2, computed for the galaxy J033230.57.

6. DISCUSSION

6.1. *Previous Detections of Extended Mg II Emission*

Previous constraints on the brightness of scattered Mg II emission were reported by Rubin et al. (2011). In this work the authors studied emission from the starburst galaxy TKRS 4389 at $z = 0.69$ with a star formation rate of 49.8 $M_\odot$ yr^{-1}. This emission was detected in a 2-dimensional Keck/LRIS spectrum, with flux from the emission reaching (8.0 ± 0.4) and $(4.4 \pm 0.4) \times 10^{-18}$ ergs sec^{-1} cm^{-2} at λ_{2796} and (4.0 ± 0.3) and (2.5 ± 0.4) $\times 10^{-18}$ ergs sec^{-1} cm^{-2} at λ_{2803} in two independent locations spatially offset from the galaxy continuum. The flux from the emission can be converted into two surface brightness values by taking the average of the flux measured at each location and each transition, and dividing by a 1 sq.arcsec aperture.

Figure 9 shows a plot of the 5σ detection limits determined for each galaxy in our sample as well as the SB calculated for the galaxy TKRS 4389 vs SFR. The figure suggests that we should be able to detect scattered Mg II emission with strengths similar to that detected in TKRS 4389. Taken at face value the figure is consistent with a positive correlation between Mg II SB and SFR.

6.2. *Geometry of Scattering Materials*

In idealized wind models of cool gas outflows, discussed in Prochaska et al. (2011), radiative transfer calculations suggest that strong Mg II emission is predicted to be generated along with ubiquitous blueshifted ab-
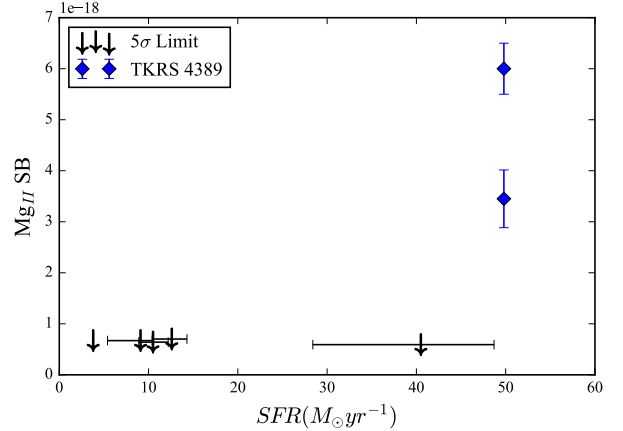

Figure 9. Comparison of our detection limits to the measured extended emission of TKRS 4389. Our imaging is sufficiently sensitive to detect extended emission at similar strengths to the extended emission measured for TKRS 4389.

sorption of Mg II. For isotropic and dust-free scenarios, photons are conserved, as any absorbed continuum photon is eventually re-emitted, most likely at a different rest wavelength, therefore the total equivalent width of both the absorption and emission feature is equal to zero in such modes. Assuming that our galaxies host an isotropic and dust-free wind, we wish to determine how much emission is predicted to be generated by this wind, and how the SB of this emission compares to our detection limits.

To calculate the predicted emission flux we first determine the flux absorbed by Mg II ions. Using our Keck/LRIS spectra, we find the average value of the continuum near the Mg II doublet and multiply this value by the observed EW of the doublet. Then to estimate the SB, we distribute this flux uniformly inside multiple annuli of varying sizes. These annuli all have an inner radius equal to the galaxy's isophotal radius and successively larger outer radii. Additionally, since our SB limits are dependent on the size of the aperture used, we calculate the SB detection limits of our images inside each of the aforementioned annuli. Figure 16 shows how the SB of emission varies with the spatial extent of the annulus (black squares), as well as how the SB compares with our detection limits (thin black curve). Excepting the galaxy J033230.03, the SB of this missing emission lie above our detection limits. Without taking into account that the emission may not exceed to a radial extent outside the galaxy disk, this result suggests that these galaxies do not host an isotropic dust-free wind.

There are many phenomena that may reduce the SB of the scattered Mg II emission so that it is consistent with

our observations. Introducing dust into the wind can reduce the observed emission strength, and shape in the line profile. In the absense of dust, the back scattered Mg II photon can escape the galaxy free of collisions. With dust, the photons are susceptible to a number of collisions, with a greater possibility of being absorbed by dust. In the Prochaska et al. (2011) radiative models with increasing dust, the dominant effect that dust has on the Mg II transitions is that the dust suppresses the most redshifted emission. The strength of the flux is reduced by a factor of $(1 + \tau_{dust})^{-1}$, where τ_{dust} is the integrated opacity of dust.

Another factor that can reduce the amount of emission is anisotropy of the wind. Isotropic winds are idealized, but galaxies are not spherically symmetric and the shape of the galaxies interstellar medium may preferentially suppress outflows at varying strengths for different galactic longitudes. We now assume that the emission in our galaxies is reduced by purely by the effects anisotropy, as the constraints on dust attenuation or unknown. For the anisotropic winds modeled in Prochaska et al. (2011), the factor that the emission is reduced is given by the scaling $\Omega/4\pi$, where Ω is the angular extent of the wind which is constrained to point towards the observer $\Omega > 2\pi$. We show the anisotropic wind SB profiles in Figure 16.

After reducing the SB of the missing Mg II emission by the minimum opening angle $\Omega = 2\pi$, we are able to profiles that fall below our SB detection limits for galaxy's J033225.26 and J033231.36. However, the SB profile of J033229.64 remains above our SB detection limits, suggesting additional phenomena are needed to reduce the strength of missing emission. Previously discussed in Section 5, this galaxy is the intrinsically brightest galaxy of our sample, which suggests a strong ISM component. Mg II photons can be more effectively trapped with the combination of ISM+dust Prochaska et al. (2011).

7. CONCLUSION

We presented the results from a narrowband imaging search for Mg II emission in a sample of star-forming galaxies at a redshift of $z \sim 0.70$ which are known to drive outflows in Mg II. We did not detect any Mg II emission in this sample, and place a 5σ detection upper limit of SB(Mg II) $\approx 5.74 \times 10^{-19}$ ergs sec^{-1} cm^{-2} arcsec^2, measured in an extended annulus outside the largest galaxy. We detected a significant amount of Mg II absorption in a total of 4 galaxies out of our 5 galaxy sample. Furthermore, our imaging allows us to generate spatially-resolved maps of Mg II absorption in a distant galaxy sample for the first time. This absorption covered the center of the galaxies out to an isopho-

tal radius defined by the SB$_1$ (1σ) depth of a continuum + Mg II image, at approximately ~ 22 kpc, suggesting that the absorbing gas fully covers the stellar disks out to this distance. The measured EWs measured in these maps are in broad agreement with measured EWs using Keck/LRIS integrated slit spectroscopy. Additionally, our radial projections of the mean EW for our sample galaxies suggest that the EWs due to Mg II are approximately constant across the galaxies surfaces.

We compared our detection limits with the prediction of the radiative transfer models of Prochaska et al. (2011). We are able to rule out that the winds in our sample are isotropic and dust free, as our images are sufficiently sensitive to detect the predicted emission from such models. By assuming anisotropic winds, we were able to reduce the strength of the predicted emission to lie below our detection limit for 3 of our sample galaxies. Albeit one galaxy that needs additional phenomena like dust to reduce the SB of emission and be consistent with our observations.

Based on the radial extent and strength of our measured Mg II absorption, the Mg II is optically thick. Deeper images in Mg II are required to observe any extended emission beyond the depth of our images. Although we are able to rule out that the winds in our sample are isotropic and dust-free, questions linger on weather the wind is anisotropic as well as dust-free. A new generation of instruments such as the Keck Cosmic Web Imager (KCWI) or the Multi Unit Spectroscopic Explorer (MUSE) should be used to answer the prevailing questions
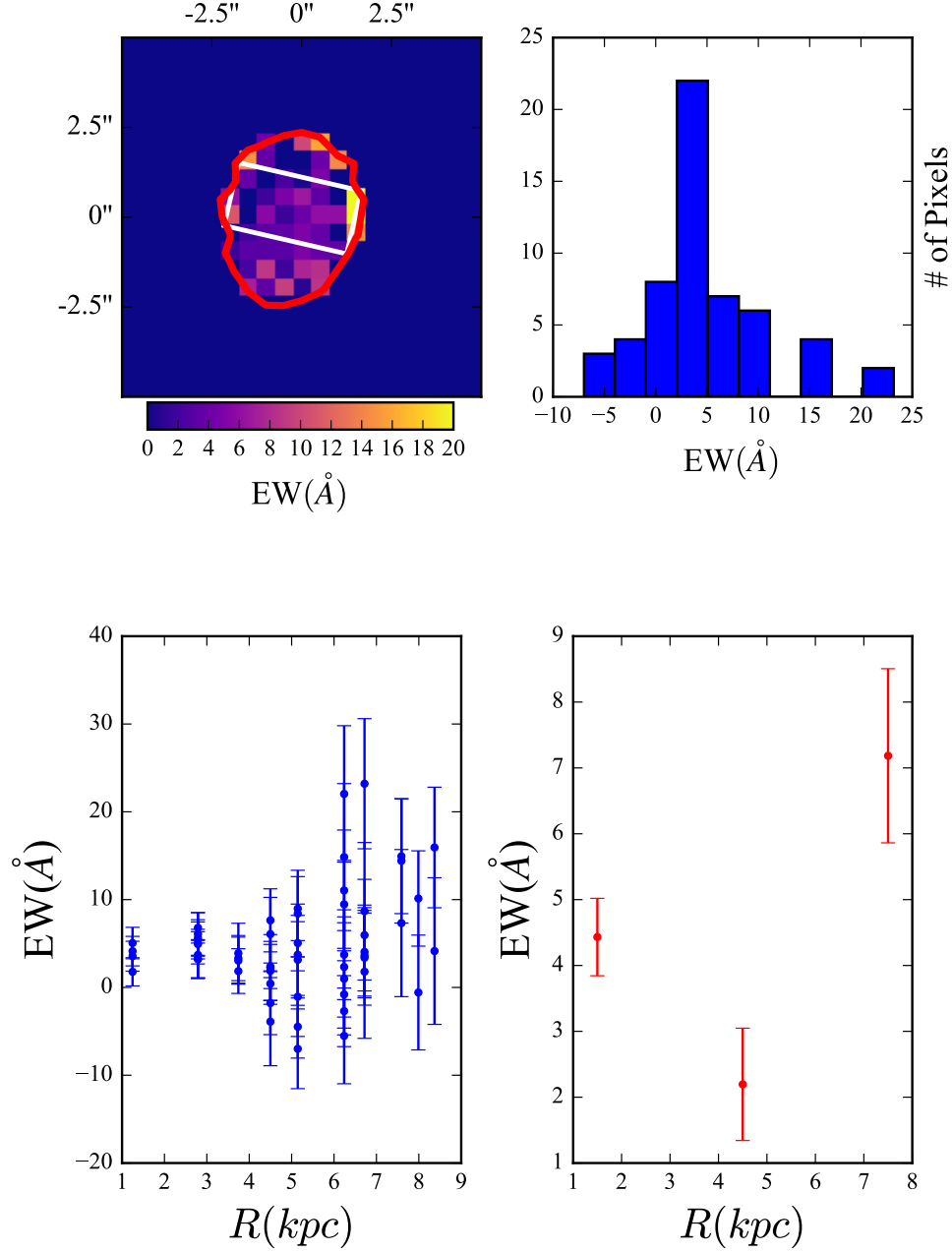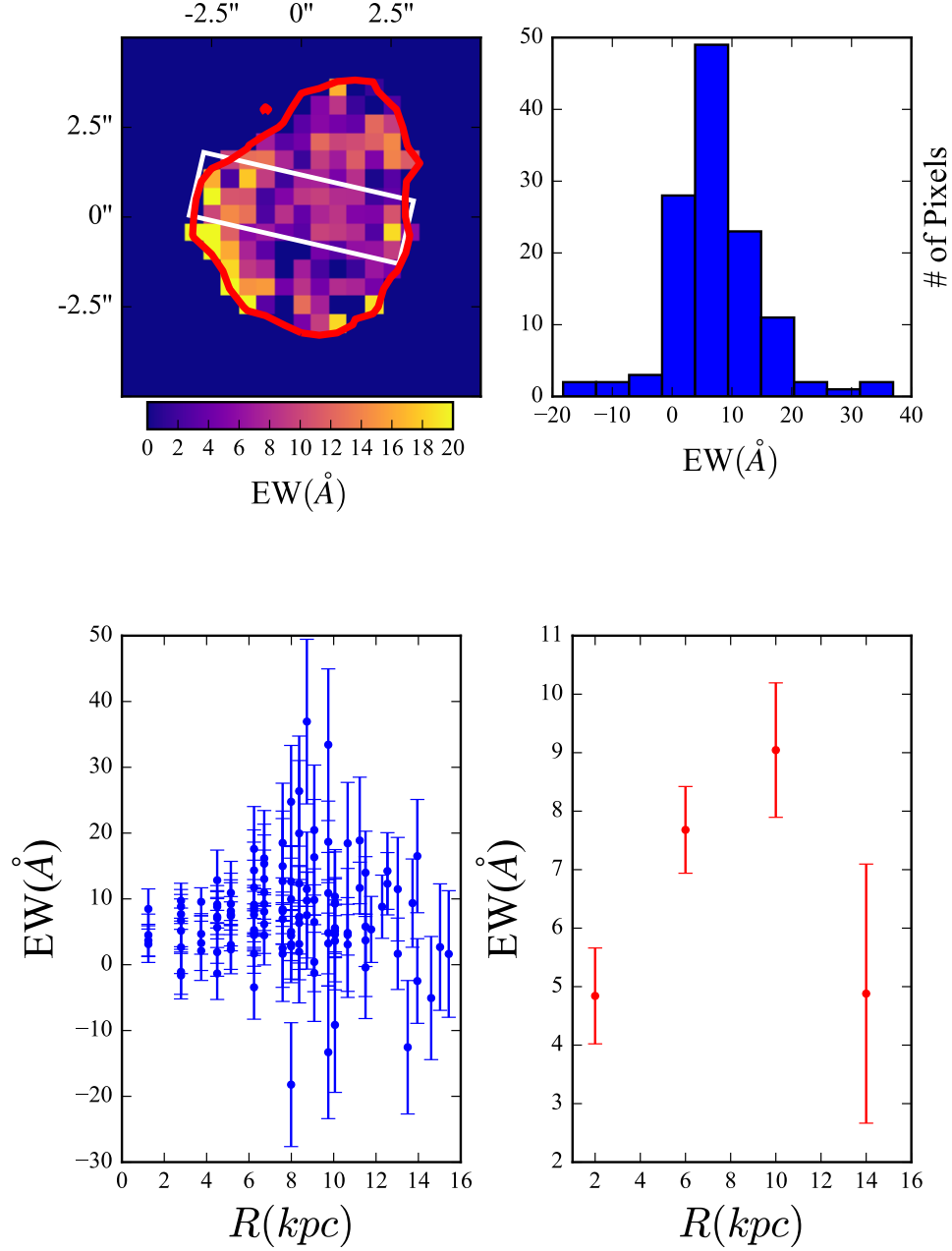
Figure 10. Equivalent width images, distribution and radial projection for J033225.26. (Top Left) image of the Mg II equivalent widths inside the red $1SB_1$ contour. The white contour represents the 0.9″ wide slit used to measure the equivalent width of absorption in the Keck/LRIS spectra. (Top Right) Distribution of absorption pixels with continuum flux S/N greater than 1.5 inside the slit aperture. (Bottom Left) The EWs of absorption vs projected distance from center. (Bottom Right) Binned EW measurements. Each point represents the mean EW measured in 3 kpc wide bins.

Table 4. Properties of Mg II Absorption

Object	Max(SB$_{abs}$)[a]	$R_{\mathrm{SB}_1}(kpc)$	EW$_{\mathrm{obs}}(\mathring{A})$[b]	EW$_{\mathrm{obs}}(\mathring{A})$[c]
J033225.26-274524.0	-5.39 ± 1.28	8	3.511 ± 0.795	7.539 ± 0.354
J033232.36-274725.0	-5.64 ± 0.121	15	7.694 ± 1.016	5.835 ± 0.493
J033230.03-274347.3	-4.41 ± 0.622	21	5.388 ± 0.712	12.79 ± 1.710
J033229.64-274242.5	-18.2 ± 0.127	10	7.546 ± 0.660	13.24 ± 0.263
J033230.57-274518.2	-1.25 ± 1.15	11	-0.6532 ± 0.589	6.106 ± 0.370

[a]SB Values are in units of 10^{-18} ergs sec $^{-1}$ cm^{-2} arcsec^2

[b] Measured from EW images

[c]Measured from Keck/LRIS spectra

Figure 11. Equivalent width images, distribution and radial projection for J033231.36. (Top Left) image of the Mg II equivalent widths inside the red 1SB$_1$ contour. The white contour represents the 0.9″ wide slit used to measure the equivalent width of absorption in the Keck/LRIS spectra. (Top Right) Distribution of absorption pixels with continuum flux S/N greater than 1.5 inside the slit aperture. (Bottom Left) The EWs of absorption vs projected distance from center. (Bottom Right) Binned EW measurements. Each point represents the mean EW measured in 4 kpc wide bins.
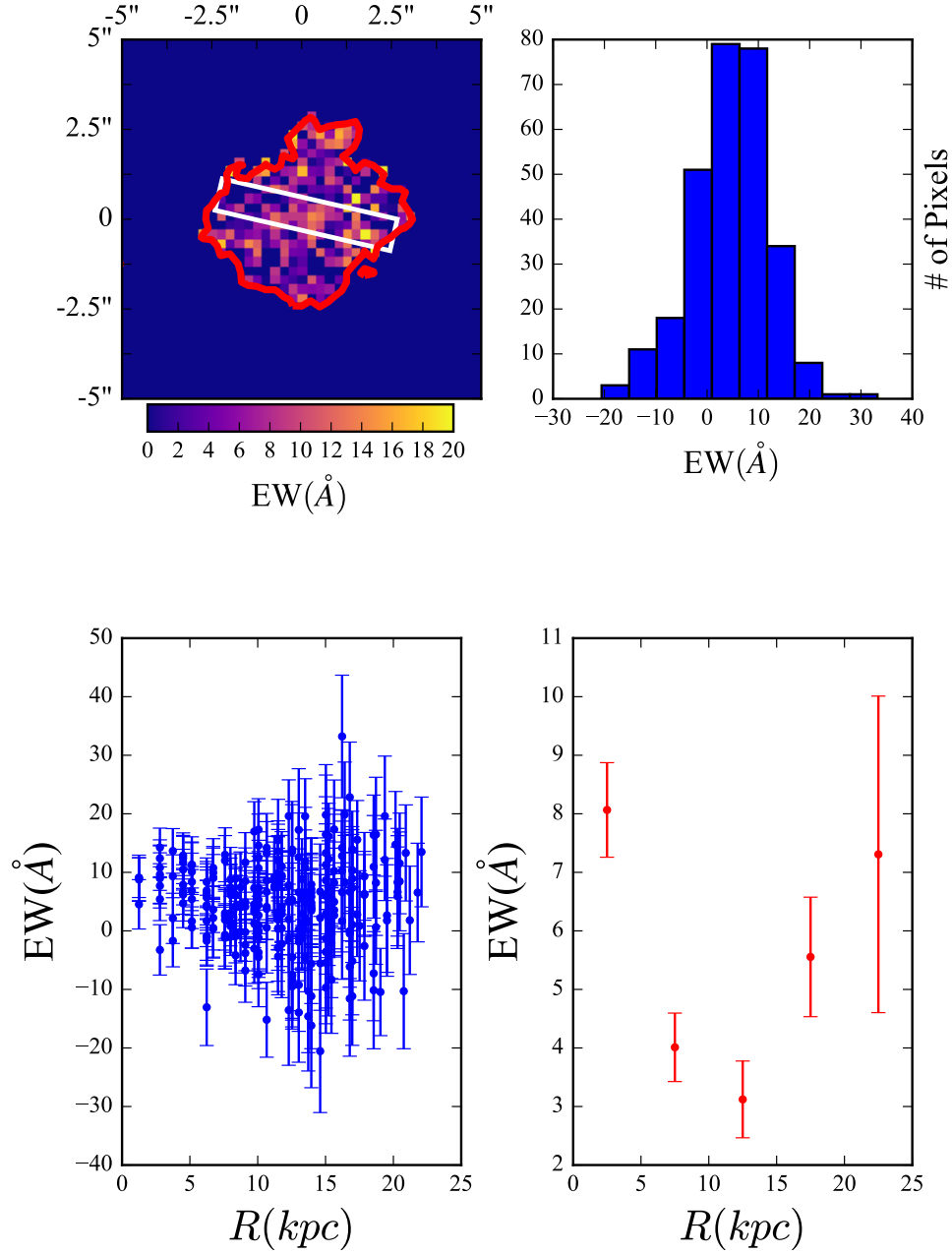
Figure 12. Equivalent width images, distribution and radial projection for J033230.03. (Top Left) Stamp of the equivalent widths (EWs) inside the red 1SB$_1$ contour. The white contour represents the $0.9''$ aperture slit used to measure the equivalent width of absorption in the Keck/LRIS spectra. (Top Right) Distribution of absorption pixels with continuum flux S/N greater than 1.5 inside the slit aperture. (Bottom Left) The EWs of absorption projected in distance from center. (Bottom Right) Binned EW measurements. Each point represents the mean EW measured in 5 kpc increment bins.
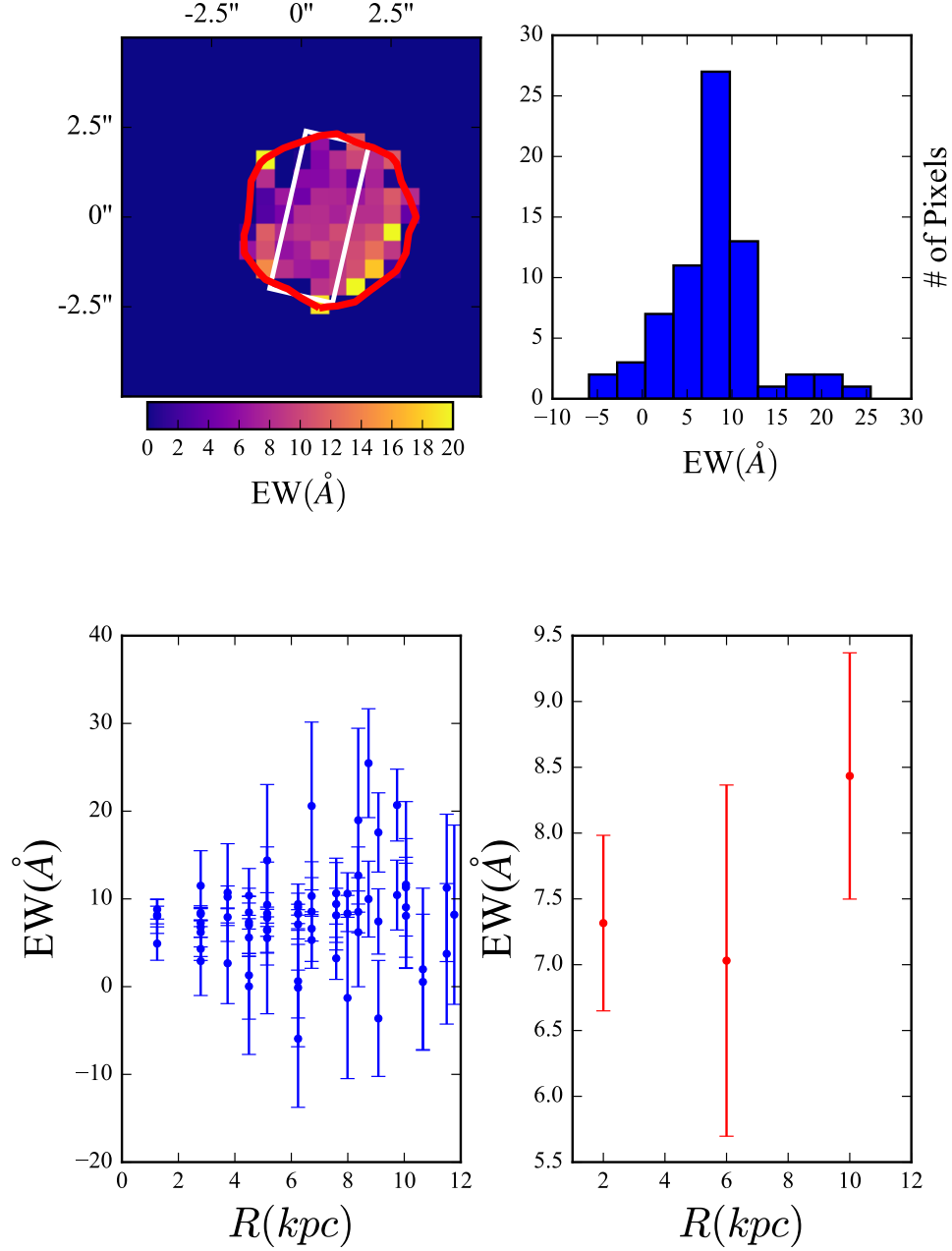
Figure 13. Equivalent width images, distribution and radial projection for J033229.64. (Top Left) Stamp of the equivalent widths (EWs) inside the red $1SB_1$ contour. The white contour represents the $0.9''$ aperture slit used to measure the equivalent width of absorption in the Keck/LRIS spectra. (Top Right) Distribution of absorption pixels with continuum flux S/N greater than 1.5 inside the slit aperture. (Bottom Left) The EWs of absorption projected in distance from center. (Bottom Right) Binned EW measurements. Each point represents the mean EW measured in 4 kpc wide bins.
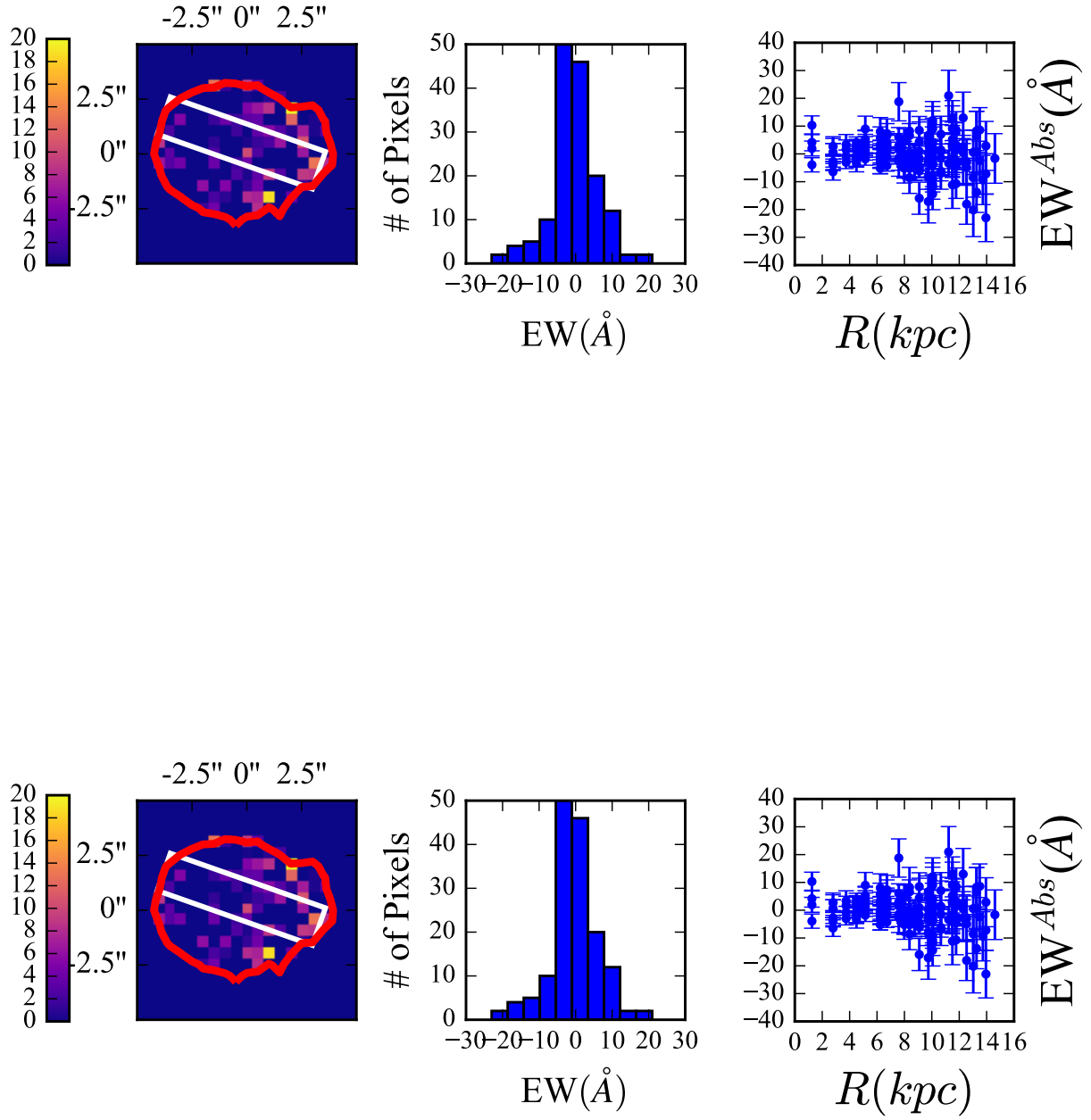
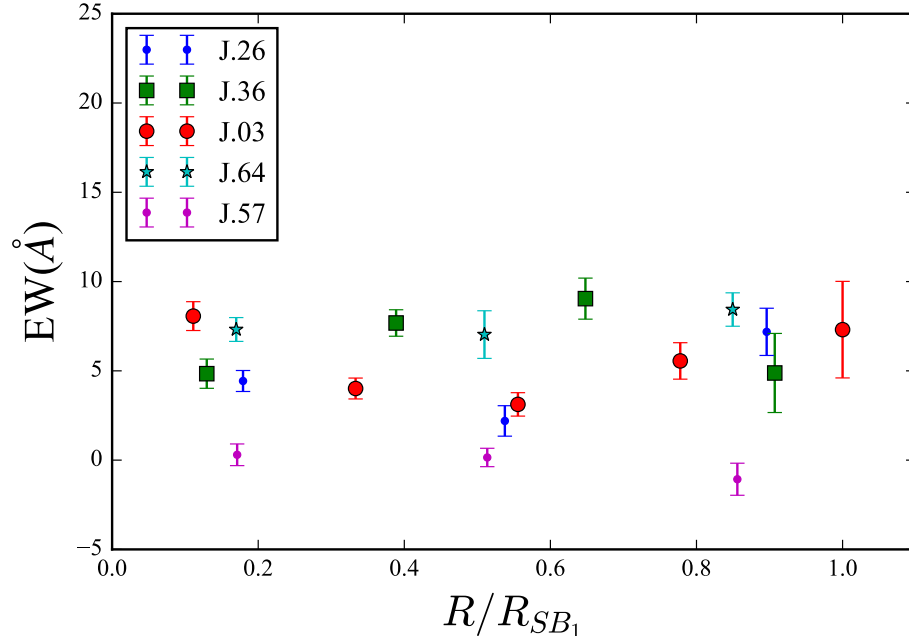**Figure 14.** Example of new figure style, Need to create for remaining galaxies

Figure 15. Normalized radial profile of the mean EW of Mg II absorption for all galaxies. Measurements for the mean EW binned in radial increments compiled to test the significance of any trends found in the individual galaxy profiles. There is significant scatter relative to the error bars at extended distances.

REFERENCES

Arrigoni Battaia, F., Yang, Y., Hennawi, J. F., et al. 2015, ApJ, 804, 26

Bertin, E., Mellier, Y., Radovich, M., et al. 1996, A&AS, 117, 393

Chen, H.-W., Wild, V., Tinker, J. L., et al. 2010, ApJL, 724, L176

Chevalier, R. A., & Clegg, A. W. 1985, Nature, 317, 44

Davis, M., Guhathakurta, P., Konidaris, N. P., et al. 2007, ApJL, 660, L1

Erb, D. K., Quider, A. M., Henry, A. L., & Martin, C. L. 2012, ApJ, 759, 26

Giavalisco, M., Ferguson, H. C., Koekemoer, A. M., et al. 2004, ApJL, 600, L93

Hennawi, J. F., & Prochaska, J. X. 2013, ApJ, 766, 58

Kornei, K. A., Shapley, A. E., Martin, C. L., et al. 2013, ApJ, 774, 50

Lang, D., Hogg, D. W., Mierle, K., Blanton, M., & Roweis, S. 2010, AJ, 139, 1782

Larson, R. B. 1974, MNRAS, 169, 229

Martin, C. L., Shapley, A. E., Coil, A. L., et al. 2012, ApJ, 760, 127

Martin, C. L., Shapley, A. E., Coil, A. L., et al. 2013, ApJ, 770, 41

Matsubayashi, K., Sugai, H., Hattori, T., et al. 2009, ApJ, 701, 1636

Prochaska, J. X. 2016, Linetools, https://github.com/linetools/linetools

Prochaska, J. X., Kasen, D., & Rubin, K. 2011, ApJ, 734, 24

Rubin, K. H. R., Prochaska, J. X., Koo, D. C., et al. 2014, ApJ, 794, 156

Rubin, K. H. R., Prochaska, J. X., Ménard, B., et al. 2011, ApJ, 728, 55

Springel, V., & Hernquist, L. 2003, MNRAS, 339, 289

Sugahara, Y., Ouchi, M., Lin, L., et al. 2017, ApJ, 850, 51

Tripp, T. M., Meiring, J. D., Prochaska, J. X., et al. 2011, Science, 334, 952

van Dokkum, P. G. 2001, PASP, 113, 1420

Veilleux, S., Cecil, G., & Bland-Hawthorn, J. 2005, ARA&A, 43, 769

Veilleux, S., Rupke, D. S. N., & Swaters, R. 2009, ApJL, 700, L149

Weiner, B. J., Coil, A. L., Prochaska, J. X., et al. 2009, ApJ, 692, 187

Werk, J. K., Prochaska, J. X., Tumlinson, J., et al. 2014, ApJ, 792, 8
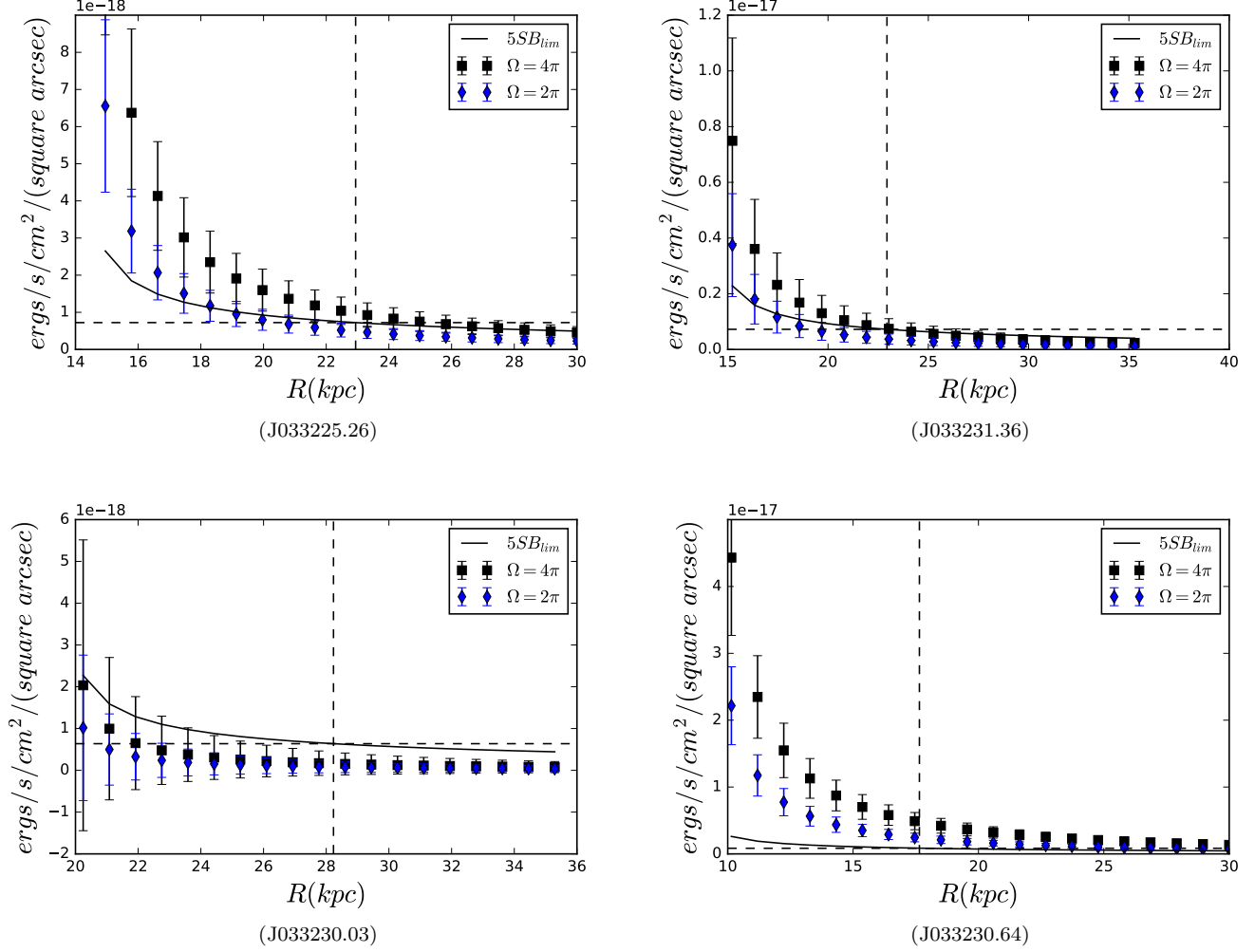
Figure 16. Estimated SB profile of Mg II emission for Isotropic and Anisotropic dust-free winds. The black square points are SB of missing Mg II emission uniformly distributed inside an annulus for an angle $\Omega = 4\pi$, or an isotropic wind. The blue diamond points are SB of missing Mg II emission uniformly distributed inside an annulus for an angle $\Omega = 2\pi$, or an anisotropic wind. The solid line shows the value of the SB detection limits. The dashed vertical and horizontal lines represent outer radius of the extended annulus use to measure the initial detection limits and the value of SB detection limit in that annulus.